43rd AIAA Aerospace Sciences Meeting and Exhibit
10-13 Jan 2005 Reno, Nevada

AIAA-2005-1110

An Isolated Circular Synthetic Jet in Cross-Flow at Low Momentum-Flux Ratio

Ivana M. Milanovic*
University of Hartford, West Hartford, CT, 06117

Khairul B.M.Q. Zaman†
NASA Glenn Research Center, Cleveland, OH 44135

and

Christopher L. Rumsey‡
NASA Langley Research Center, Hampton, VA, 23681

A joint experimental and computational investigation was carried out for a round synthetic jet issuing normal to a turbulent boundary layer at a momentum-flux ratio of one. Distributions of velocity and turbulence intensity were measured by hot-wire anemometry. Numerical results were obtained using unsteady Reynolds-averaged Navier-Stokes (URANS) computations. Time and phase-averaged flow properties were compared on the cross sectional plane at x/D = 0.53, 5 and 10 as well as on the axial plane of symmetry. Overall, the numerical results agreed well with the experimental data. CFD predicted a somewhat larger velocity deficit in regions of low-momentum fluid pulled up from the boundary layer. Phase-averaged velocity contours at the plane of symmetry indicated good match between experiments and CFD regarding the size and the position of the periodic flow structure. However, some differences occurred in details such as the shape and inclination of the low-speed flow structure.

Nomenclature

D = diameter of orifice
f = forcing frequency
J = momentum-flux ratio,
L_0 = stroke length,
t = time
T = forcing period,
v_0 = velocity at exit center of orifice (at $x = y = z = 0$)
V_0 = velocity during discharge cycle averaged over entire period,
U, V, W = mean velocity in streamwise, normal, and spanwise directions
u', v', w' = turbulence intensities in streamwise, normal and spanwise directions
= turbulent shear stresses in steamwise, normal and spanwise directions
x, y, z = Cartesian coordinates in streamwise, normal and spanwise directions

* Assistant Professor, Department of Mechanical Engineering, 200 Bloomfield Av., Member AIAA.
† Aerospace Engineer, Propulsion Systems Division, Nozzle Branch, Mail Stop 86-7, Associate Fellow AIAA.
‡ Research Scientist, Computational Modeling and Simulation Branch, Mail Stop 128, Associate Fellow AIAA.

I. Introduction

A synthetic jet is formed when an oscillating pressure field is imposed across an orifice. This may be achieved with a closed cavity and a vibrating membrane placed on one side of the orifice plate. Forced motion of the membrane results in a time-periodic suction and blowing through the orifice. During suction fluid is entrained into the cavity. Subsequent discharge forces out a layer of vorticity that then rolls up into a vortex ring while entraining the surrounding fluid. Self-induction propels the vortex away from the plate. Consequently, a jet is 'synthesized,' entirely out of the ambient fluid, by the train of discrete vortices. The resultant flowfield becomes similar to that of a steady jet just a few diameters away from the orifice.[1]

The first radio receivers with a loudspeaker in the thirties were known to produce 'loudspeaker wind.'[2] Acoustic streaming,[3,4] the underlying mechanism of synthetic jets, has been known to aeroacoustians since the fifties. However, several recent studies including those of Smith and Glezer[1,5] and Glezer and Amitay[6] uncovered the potential of the synthetic jet as a flow control device. Since a synthetic jet has zero-net-mass-flux it is attractive for flow control. It brings forth the possibility of 'fluidic injection' and periodic perturbation without the requirement of bleed fluid and the associated hardware. When applied to various propulsion components synthetic jets have been shown to produce a range of beneficial effects.[7-15] They can prevent boundary layer separation, reduce losses and increase volume flow rate in duct flows, alter aerodynamic characteristics of lifting surfaces, enhance mixing in continuous jets as well as reduce blade vortex interaction noise.

While a host of previous studies addressed the dynamics of a synthetic jet issuing into a quiescent ambient, research and databases with the addition of a cross-flow (SJCF) have been rather limited. Gordon and Soria[16] studied circular SJCF with particle image velocimetry (PIV) and compared them to steady and pulsed jets in cross-flow. Velocity ratios ($VR = U_j/U_\infty$) of 4.6 and 7 were investigated, where 'jet velocity' U_j was based on the average momentum discharged through the orifice and U_∞ was the freestream velocity. The results suggested similarity of the SJCF to free synthetic jets close to the orifice and to pulsed jets farther downstream. Jet penetration was comparable to that reported for a continuous jet in cross-flow. Schaeffler[17] used PIV to document the interaction of a round synthetic jet with turbulent boundary layer in the vicinity of the orifice at velocity ratios of 0.36, 0.48 and 0.95. 'Jet velocity' was defined as the root-mean-square of velocity over a complete cycle. Reduced penetration with increased freestream Mach number was noted and complex interactions during the roll-up were elucidated. In Ref. 18 round SJCF's were studied with hot-wire anemometry at jet Reynolds number (Re) up to 23,000 and Stokes number (S) up to 400. Re and S were based on characteristic velocity ($2V_0$) and orifice diameter. Distributions of mean velocity, streamwise vorticity, turbulence intensity and SJCF trajectory were documented and found to be quite similar to those of a steady jet-in-cross-flow. Gordon et al.[19] applied planar-laser-induced fluorescence to investigate SJCF for a range of Strouhal numbers ($0.005 \leq St \leq 0.077$) and Reynolds numbers ($600 \leq Re \leq 23{,}200$) as well as velocity ratios ($3 \leq VR \leq 30$). Re and St were based on jet velocity and orifice diameter. Two flow regimes were observed that involved single and multiple trajectories of the SJCF. A critical Strouhal number of 0.02 distinguished the two regimes. All of the cited studies employed sinusoidal signals as forcing functions.

The current work was undertaken as a follow-up study to Ref 18. Detailed flowfield data were documented for a specific case of a round SJCF at a momentum-flux ratio of one. The intent was to complement the database for a CFD workshop ('case 2'; Refs. 20-22) held on the subject at NASA LaRC in March, 2004. The computational simulation was performed by the third coauthor based on the present dataset. The purpose of this paper is to document and provide an analysis of the experimental results and to discuss the highlights of the computational results. Details of the numerical simulation on both the current case and 'case 2' will be presented in a later paper.[23]

II. Procedures

A. Experimental Procedure

The experiments were conducted in a NASA Glenn Research Center open-circuit low-speed wind tunnel with a 30 in. wide x 20 in. high test section. The wind tunnel had a 16:1 contraction section at the inlet with the fan located at the downstream end. The setup is shown schematically in Fig. 1. The orifice, with diameter $D = 0.75$ in., was cut in a 10 in. diameter by 1 in. thick plate. The plate was mounted flush on the test section floor with the orifice placed at the tunnel centerline. The synthetic jet was produced by a 14 in. woofer (Altec Lansing) housed in a chamber underneath the test section. The chamber was 6 in. deep with a volume of about 1700 in^3. The Helmholtz resonance of the chamber/orifice was 24 Hz. The experiment was conducted at the resonant frequency with a sinusoidal function driving the woofer.

The measurements were performed by hot-wire anemometry. The characteristics of the oscillatory flow at the orifice exit were evaluated with a single element hot-wire. The detailed data on the cross-sectional plane at various streamwise locations were acquired using two adjacent ×-film probes (TSI 1241-20), one placed in 'u-v' and the

other in *'u-w'* orientation. The probes were traversed under automated computer control through the same grid points allowing the measurement of all three components of mean velocity and turbulence intensity. Gradient-correction was applied to v and w components. The details of the probe calibration and uncertainty estimates can be found in Ref. 24. The uncertainties in the normalized streamwise velocity (u) and vorticity ($\_x$) were estimated to be within 2% and 20%, respectively. The origin of the coordinate system is located at the center of the orifice as illustrated in Fig. 1. The streamwise (i.e. cross-flow) direction is denoted by x, the direction normal to the tunnel floor is denoted by y, and the spanwise direction by z.

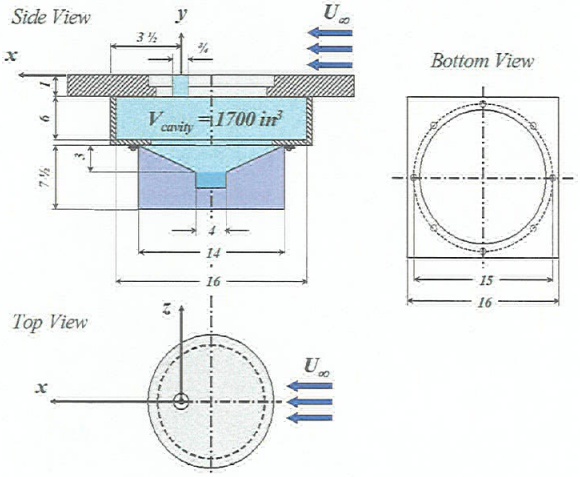

Fig. 1 Experimental set up: loudspeaker, cavity and orifice configuration.

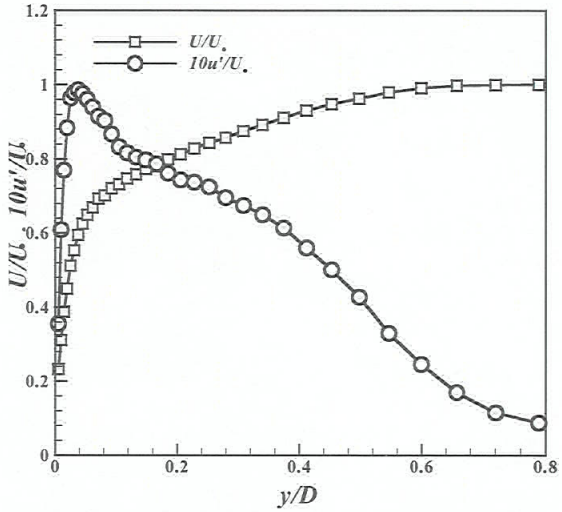

Fig. 2 Approach boundary layer profiles at $x/D = -5.2$, $z/D = 0$.

A saw-tooth boundary layer trip was applied $11D$ downstream from the beginning of the test section and $17D$ upstream of the orifice. The approach boundary layer was turbulent with a thickness of $0.6D$, as seen in Fig. 2. The Reynolds number was 7530 based on D and V_{max}. The following parameters characterized the flowfield under consideration: maximum discharge velocity, $V_{max} \approx$ 20 ft/s, characteristic velocity,[1] $V_0 \approx$ 6.4 ft/s, and non-dimensional stroke length, $L_0/D \approx 4.3$. The cross-flow velocity was $U_\infty \approx$ 20 ft/s; thus, / .

B. Numerical Procedure

The numerical simulation used the CFL3D code.[25] The CFL3D code solves the three-dimensional, time-dependent, compressible Reynolds averaged Navier-Stokes (RANS) equations with an upwind finite-volume formulation. Upwind-biased spatial differencing is used for the inviscid terms. Viscous terms are centrally differenced, and cross-diffusion terms are neglected. For very low Mach number flows such as the current case, preconditioning[26] is used to insure convergence and accuracy of the solutions. The code is advanced in time with an implicit approximate factorization method. The implicit derivatives are written as spatially first-order accurate, which results in block tridiagonal inversions for each sweep. However, for solutions that utilize Roe flux-difference splitting,[27] the block tridiagonal inversions are further simplified using a diagonal algorithm with a spectral radius scaling of the viscous terms.

In time-accurate mode (unsteady RANS or URANS), CFL3D uses pseudo-time stepping with multigrid and achieves second order temporal accuracy. With pseudo-time stepping, subiterations are used to reduce the linearization and factorization errors, and advance the solution in pseudo time to the next physical time. The turbulence models are solved uncoupled from the mean flow equations using implicit approximate factorization. The one-equation model of Spalart-Allmaras[28] is used in the current study. This model is a linear eddy-viscosity model that makes use of the Boussinesq eddy-viscosity hypothesis. Further details of the code and the procedures can be found in Refs. 23, 25 and 29.

The present case was computed at the free stream Mach number, M = 0.0175. A time step corresponding to 720 steps per period was used, and 10 subiterations were employed per physical time step. Earlier studies by Rumsey[29] on a similar configuration indicated that this time step and number of subiterations were sufficient for numerical accuracy. The cavity was not modeled computationally due to its large dimensions relative to the orifice. Consequently, the grid included the orifice only, which extended 25.4 mm below the tunnel floor. The 6-zone grid

with 1-to-1 connectivity had 1.8 million total grid points, covering half of the domain (symmetry conditions were imposed on the center-plane). The approximate grid extent was $6D$ upstream, $19D$ downstream, $6D$ to the side, and $12D$ high. The case was run both on the fine grid, as well as on a coarser grid using every other point in each coordinate direction in order to investigate the grid sensitivity of the solution.

A time-dependent membrane oscillation was replaced with a time-dependent velocity boundary condition applied at the bottom of the orifice. The velocity boundary condition was determined iteratively, in order to approximately match the measured velocity as a function of phase at the orifice exit. The prescribed time-dependent vertical velocity was:

where . Upstream boundary conditions were set to approximately match the turbulent boundary layer thickness (Fig. 2), and turbulence boundary conditions were set to insure a fully turbulent inflow boundary layer profile. The tunnel floor and the walls of the orifice were modeled as adiabatic solid walls. Far field boundary conditions were set on other boundaries.

III. Results and Discussion

Phase-averaged hot-wire output on the axis of the orifice with and without the cross-flow is shown in Figs. 3(a) and (b), respectively. The peak on the right in Fig. 3 (a) represents discharge half of the cycle. The peak on the left is 'rectified' hot-wire output during suction, its magnitude approaching 'discharge' value when the probe is positioned inside the orifice. The left peak is recognized as suction from the fact that it rapidly diminishes as the probe is drawn away, since the synthetic jet gathers a mean speed. When the mean speed is zero the 'hot-wire output' equals the resultant of u- and v-components (total velocity; assuming $w = 0$). With the onset of the cross-flow, maximum discharge velocity does not change appreciably, as can be seen in Fig. 3(b). However, a double hump in the rising portion of the signal appears. A similar double hump, somewhat less pronounced, was also seen at other operating conditions.[18] In Fig. 3(b), probe positions inside the orifice resulted in larger peaks during suction. The reason for this remains unclear. The maximum amplitude during the discharge was utilized to estimate characteristic velocity and stroke length assuming a sinusoidal function. As stated earlier, all data were acquired at $f = 24$ Hz with an amplitude such that the maximum discharge velocity, $V_{max} \approx 20$ ft/s (6.1 m/s). This yielded a non-dimensional stroke length, $L_0/D \approx 4.3$. The cross-flow velocity, $U_\infty = 20$ ft/s (6.1 m/s) and orifice diameter, $D = 0.75$ in (19 mm) have been used for normalization of all data in the following.

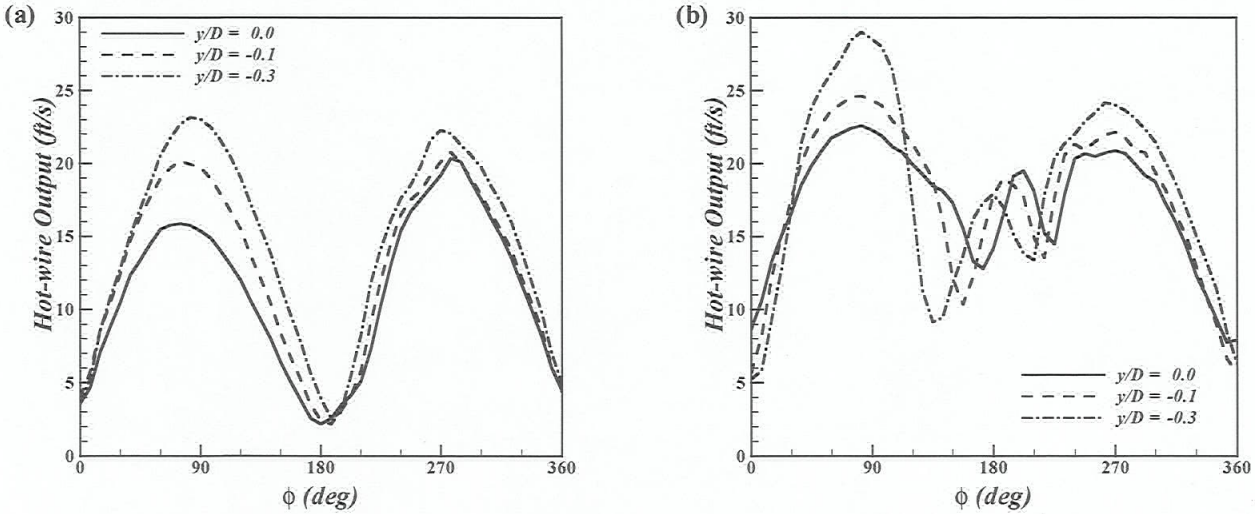

Fig. 3 Phase-averaged hot-wire output (total velocity) on the axis of the orifice at indicated y locations: (a) without cross-flow ($U_\infty = 0$), (b) with cross-flow ($U_\infty = 20$ ft/s).

Vertical profiles measured at various downstream locations are presented in Fig. 4. Profiles of mean velocity are shown in Fig. 4(a). Corresponding turbulence intensity (u') and fundamental intensity ( ) data are given in Figs.

4(b) and (c). A step-like behavior is developed in the U-profiles at about one diameter away from the orifice. These profiles exhibit an inflection point that progressively shifts upward with increasing x. The turbulence is high and remains practically constant throughout the region of lower U, dropping off sharply as U approaches U_e. The fundamental intensity was measured by on-line spectral analysis of the hot-wire signal. The drop-off in u' coincides with the occurrence of a peak in the -profile. The location of -peak provides a measure of the penetration of the SJCF. Trends in the profiles of Fig. 4 with increasing x/D resemble those that occur at a given location with increasing L_0/D.[18] This is due to the fact that SJCF penetration increases with an increase in either x or L_0.

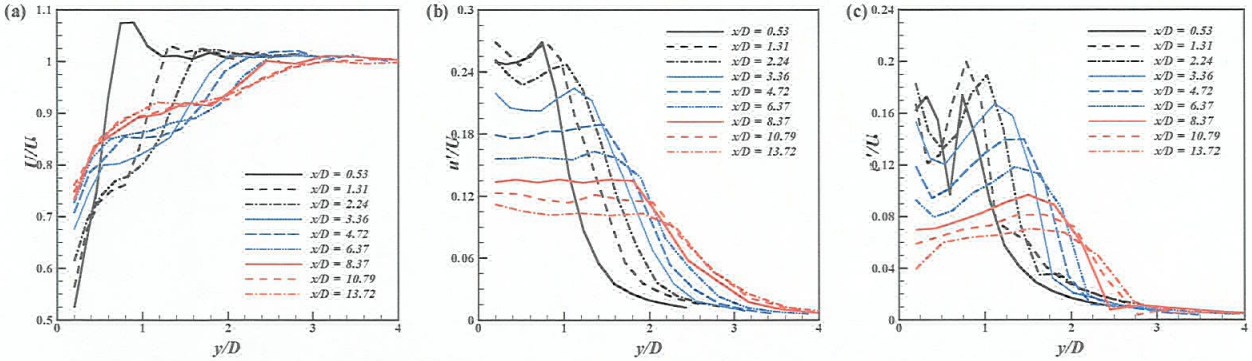

Fig. 4 Experimental profiles of (a) mean velocity, (b) turbulence intensity, and (c) fundamental intensity. Data are for plane of symmetry at indicated *x/D*.

Computed total velocity and its components corresponding to the experimental data of Fig. 3(b) at $y = 0$ are shown in Fig. 5. Two different grids, fine and coarse, yielded similar results; this attests to the sufficiency of grid density. The numerically obtained total velocity agrees very well with the experimental data. The computations accurately capture the double hump during the discharge half of the cycle. The largest discrepancy is in the magnitude of the peak during the suction half of the cycle. As indicated earlier, with a non-zero mean (likely at $y = 0$) the total velocity measured during the suction is erroneous. The CFD does show a higher magnitude in the suction half, consistent with experimental data within the orifice seen in Fig. 3(b). In Ref. 18, it was speculated that the additional peak on the left of the discharge half might be due to the cross-flow sweeping over the probe at a phase when the velocity of the synthetic jet is negative. If this were true, the double-hump should have appeared only in the u-component. The CFD v-component also exhibits a corresponding undulation during the discharge. This seems to refute the hypothesis and the reason for the complex response to forcing with the cross-flow on remains unclear at this time.

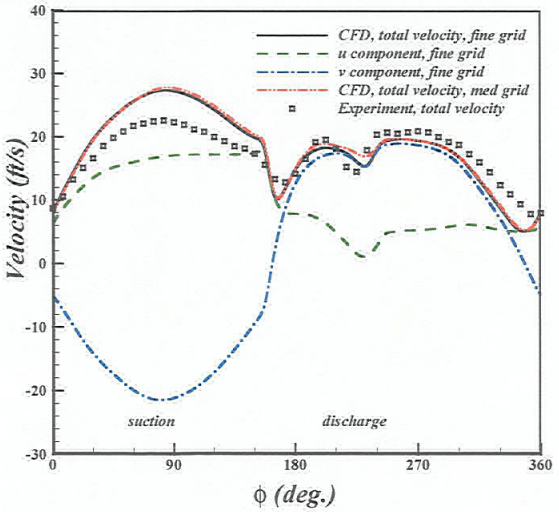

Fig. 5 Computed total velocity and its components corresponding to the data of Fig. 3b.

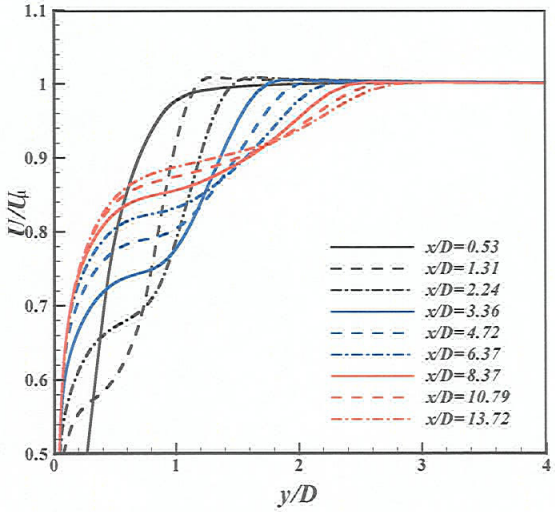

Fig. 6 Computed profiles of mean velocity at locations corresponding to profiles of Fig. 4a.

Computed profiles of mean velocity corresponding to those in Fig. 4(a) are shown in Fig. 6. A step-like behavior is also seen in the U-distributions at about one diameter away from the orifice. Discrepancy between CFD and

experimental results is observed in the location of the inflection point and accompanying velocity magnitude. For example, at x/D = 1.31, CFD yields an inflection point at y/D = 0.32 with U/U_∞ = 0.57, while corresponding experimental values are 0.75 and 0.76, respectively. Nevertheless, the general trends of fuller velocity profiles close to wall and the inflection point shifting up with increasing x are well predicted.

Time- and phase-averaged distributions of streamwise velocity are now compared. Time-averaged velocity, on the plane of symmetry and on the cross-sectional plane at x/D=5, are shown in Figs. 7 and 8, respectively. The qualitative agreement between CFD and experiment is obvious. In Fig. 7, the measurement domain ranges from just downstream of the edge of the orifice up to about 15D, while computational results are shown starting at the orifice centerline. Closer examination indicates that numerical results exhibit larger velocity defects close to the orifice and near the wall. Consequently, a discrepancy between the shape and position of a given contour line is observed.

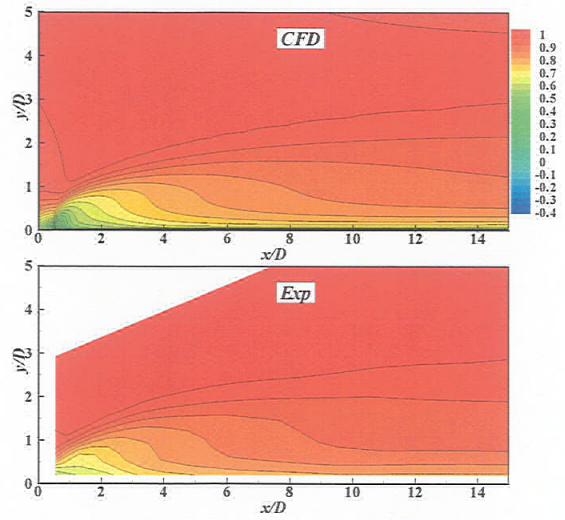

Fig. 7 Mean streamwise velocity (U/U_∞) on the plane of symmetry (z = 0).

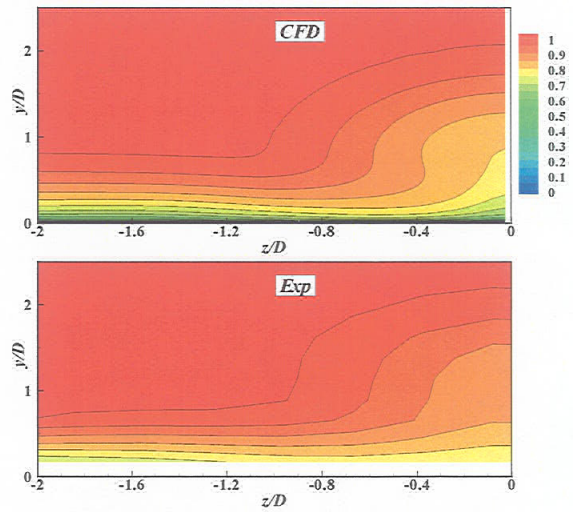

Fig. 8 Mean streamwise velocity (U/U_∞) at x/D = 5.

The unsteady character of the SJCF is captured with distributions of phase-averaged streamwise velocity. Experimental data were acquired with the same ×-wire technique for a total of 19 phases within the cycle. The distributions are shown in Fig. 9 for approximate phases of 0, 80, 160, 240, and 320 degrees from an arbitrary reference within the cycle. The periodic passage of the synthetic jet structure can be seen. While the non-dimensional stroke length is 4.3, the 'wavelength' is about 10D. The latter corresponds to a convection speed of about 0.75U_∞. For each phase, the CFD result is directly compared. There is good agreement between the size and position of the disturbance as it convects downstream after being emitted from the orifice. Dramatic changes in the velocity magnitude occur during the cycle. As with the time-averaged simulations, CFD predicts lower deficits in low-momentum fluid. Also, the low-momentum structures obtained experimentally are tilted more in the direction of convection while their numerical counterparts are upright.

Time- and phase-averaged measurements and computational simulations were performed for three cross-sectional planes at x/D = 0.53, 5 and 10. The experiments covered full cross-sectional plane and there was good symmetry about z = 0. Data on one half are shown to be consistent with the CFD that utilized the symmetry condition. Mean velocity distributions at x/D = 5, shown in Fig. 8, illustrate that a 'dome' of low momentum fluid is pulled up from the boundary layer. At low momentum-flux ratios such as in the current case, the dome is still connected with the boundary layer stretching up to about 2D from the wall. Both experiment and CFD yield the same general picture of the cross-flow. Again, lower velocity magnitudes in the dome have been predicted by the CFD. Consequently, the contour values and their spatial spread are somewhat different for the CFD case.

Phase-averaged streamwise velocity contours at x/D = 5, corresponding to the phases of Fig. 9, are shown in Fig. 10. Dramatic changes take place within the discharge half of the cycle. Velocity magnitudes and shape of periodic flow structure differ significantly from phase to phase. At 80 deg. phase shown in Fig. 10(b) the dome has almost separated from the boundary layer. This particular snapshot of the flowfield resembles the time-averaged data at a

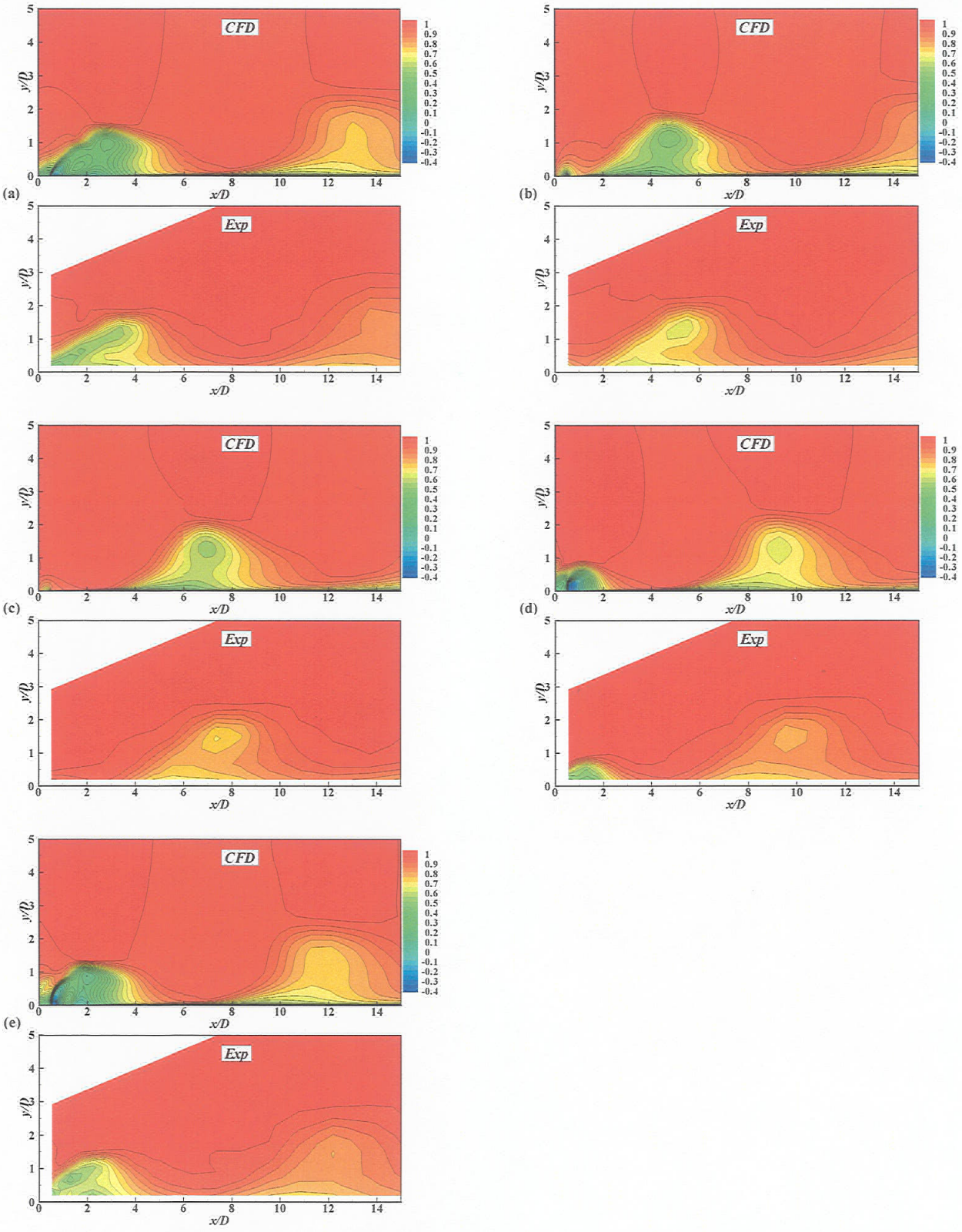

Fig. 9 Phase-averaged streamwise velocity contours on plane of symmetry. Approximate phases are (a) 0, (b) 80, (c) 160, (d) 240, and (e) 320 degrees from an arbitrary reference within the oscillation cycle.

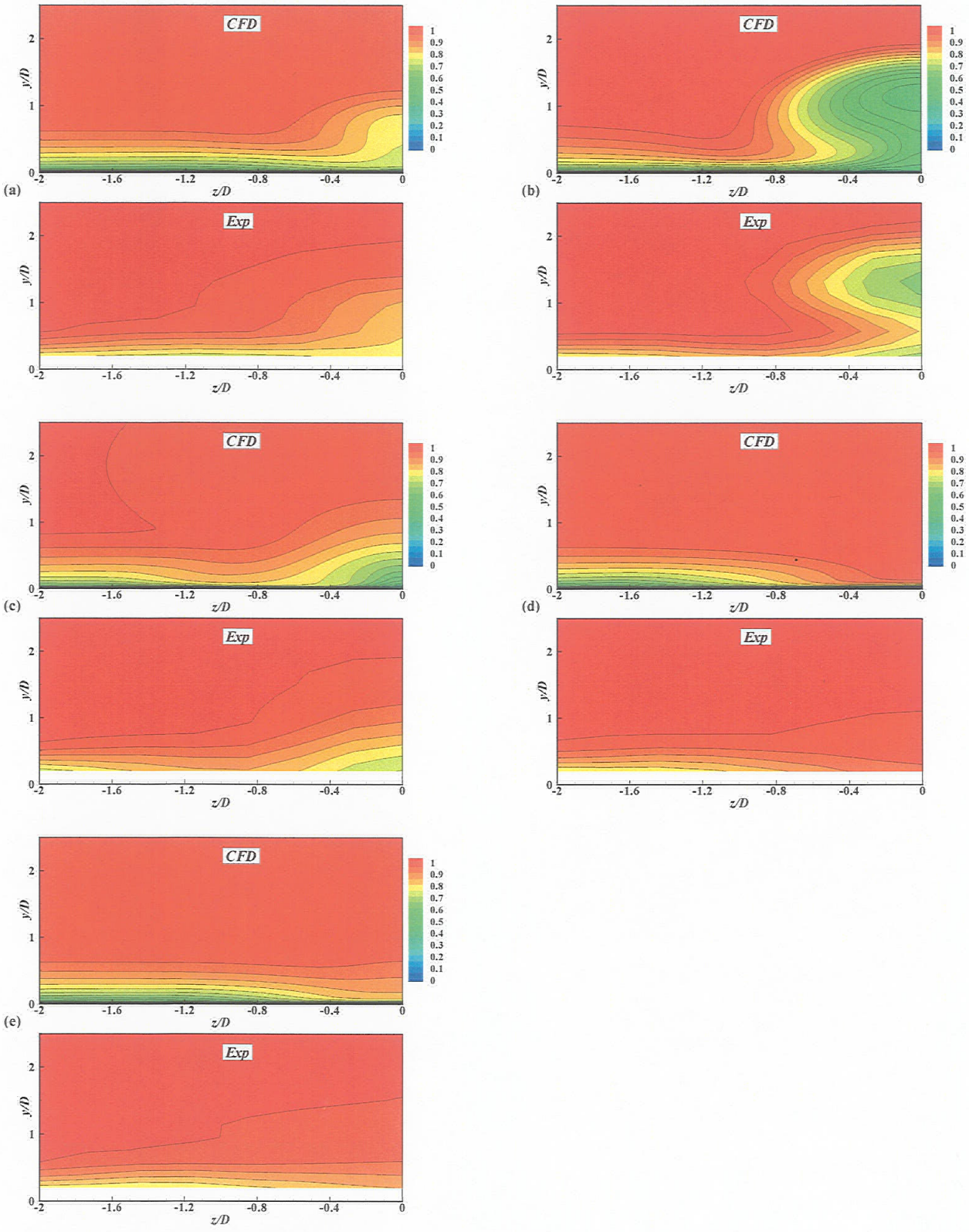

Fig. 10 Phase-averaged streamwise velocity contours on the cross-sectional plane at $x/D = 5$ corresponding to the phases of Fig. 9.

higher J where the dome is lifted and reshaped into a 'puff' hovering above the boundary layer. Dynamic topological alternations within the discharge part of the cycle, and their similarity to the time-averaged data at various momentum-flux ratios were also noted in the study of SJCF from rectangular orifices.[30] CFD has again captured these variations quite well for each phase.

Cross-sectional distributions of streamwise mean velocity only, at x/D = 0.53 and 10, are shown in Figs. 11 and 12. Comparison with Fig. 8 provides an idea about the downstream evolution of the SJCF. Both measurements and numerical simulations indicate that the dome penetrates higher with increasing x. In addition to velocity undershoot, CFD also exhibits a 'kink' in the contours close to the orifice. The reasons for the differences in these details remain unclear.

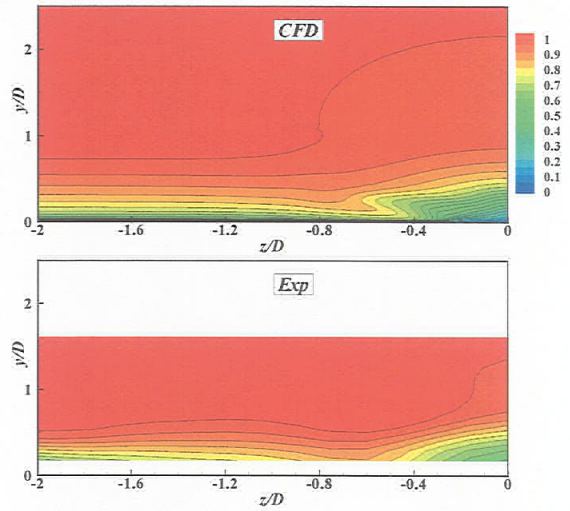

Fig. 11 Mean streamwise velocity (U/U_∞) at x/D = 0.53.

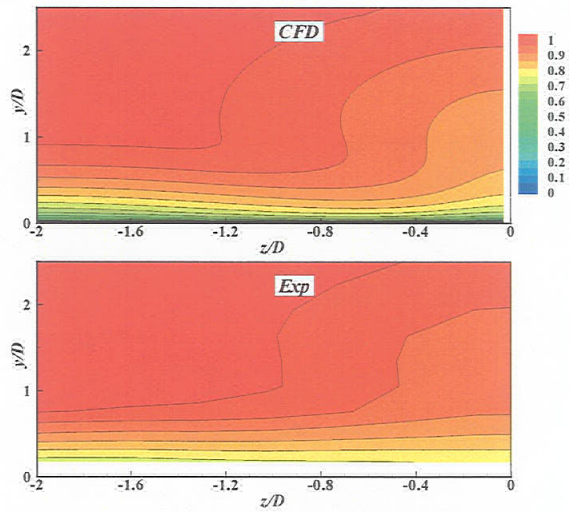

Fig. 12 Mean streamwise velocity (U/U_∞) at x/D = 10.

The experimental data also included other properties such as turbulent stresses at all measurement planes. The CFD generated turbulent stresses at specific phases only. Mean turbulent stresses were not computed for this study. The experimentally obtained stresses corresponding to the domain of Fig. 8 are presented in Fig. 13. Recall that the dome of low momentum fluid is still connected to the boundary layer and is about 2D high. Streamwise turbulence distribution in Fig. 13(a) extends farther up, to about y/D = 2.8. The dome based on the u'-data has also lifted up. Peak u' intensity of about 0.178 is found at y/D = 1.33. Turbulence intensities, v' and w', are shown in Figs. 13(b)-(c), respectively. Their peak amplitudes, in comparison with u', are found closer to the wall and are smaller by about 40%. Non-homogeneity in the normal stresses was not accounted for in the particular turbulence model used in the computations. It is possible this might have led to some of the differences between CFD and experiment seen in earlier figures. Reynolds stresses, documented in Figs. 13(d)-(e), indicate a more vigorous upward turbulent transport of momentum than in the lateral direction. Finally, streamwise vorticity, obtained from the gradients of v and w distributions, are shown in Fig. 13(f). The distributions of vorticity as well as the stresses, being derivatives of the primary quantities, are rather 'noisy.' The vorticity data have suffered more apparently due to imperfect gradient-correction in the boundary layer. Nevertheless, a pair of counter-rotating vortices, similar to the 'bound vortex pair' of a steady jet-in-cross-flow, is clearly observed.

IV. Conclusion

Qualitative similarities between experimental and computational results for the flowfield of a synthetic jet in cross-flow, at a momentum-flux ratio of one, are observed. The time-averaged velocity distributions provide the same general picture of the flow. The flowfield extents, both in transverse and streamwise directions, as well as the transverse profiles of mean velocity are fairly reproduced by the CFD. Phase-averaged data show good match regarding the size and the position of the synthetic jet structure. Dramatic changes are observed within the cycle. During the 'discharge', velocity magnitudes and flowfield topology differ considerably from phase to phase. These are captured quite well by the CFD. There are differences in the detailed comparisons. CFD overpredicts the velocity deficits in regions where the low-momentum boundary layer fluid is pulled up. The synthetic jet structures,

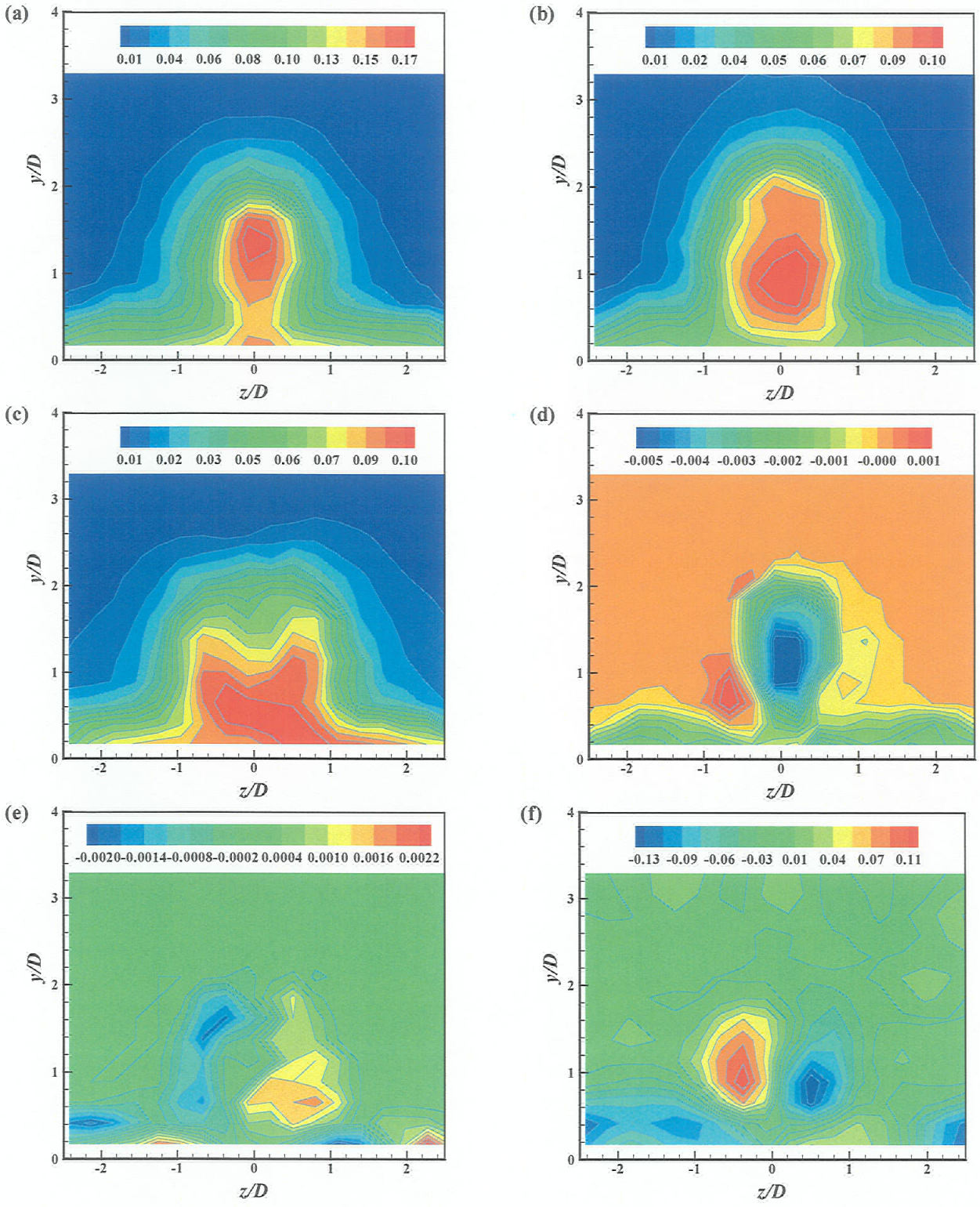

Fig. 13 Turbulence intensities, (a) u'/U_∞ , (b) v'/U_∞, and (c) w'/U_∞, Reynolds stresses, (d) $\overline{}$, and (e) $\overline{}$, and (f) mean streamwise vorticity at $x/D = 5$.

as indicated by the phase-averaged velocity contours, are tilted in the direction of convection with increasing distance away from the wall. This tilt is seen to be less pronounced in the CFD results.

Acknowledgments

The work was supported by NASA-Ohio Aerospace Institute (OAI) Collaborative Aerospace Research and Fellowship Program. The first author is grateful to Connecticut Space Grant College Consortium – The Experimental Program to Stimulate Competative Research (EPSCoR) Core Funding for providing support.

References

[1]Smith, B. L., and Glezer, A., 'The Formation and Evolution of Synthetic Jets,' *Physics of Fluids*, **10**(9): 2281-2297, 1998.

[2]Travnicek, Z., and Tesar, V., 'Annular Synthetic Jet Used for Impinging Flow Mass-Transfer,' *International Journal of Heat and Mass Transfer*, **46**: 3291-3297, 2003.

[3]Ingard, U., and Labate, S., 'Acoustic Circulation Effects and the Nonlinear Impedance of Orifices,' *J. Acous. Soc. Am.*, **174**(1): 211-218, 1950.

[4]Lighthill, M.J., 'Acoustic Streaming,' *J. Sound & Vibration,* **61**(3), 391-418, 1978.

[5]Smith, B. L., and Glezer, A., 'Jet Vectoring Using Synthetic Jets,' *Journal of Fluid Mechanics*, **458**:1-34, 2002.

[6]Glezer, A., and Amitay, M., 'Synthetic Jets,' *Annual Review of Fluid Mechanic*, **34**: 503-529, 2002.

[7]Amitay, M., Smith, D. R., Kibens, V., Parekh, D. E., and Glezer, A., 'Modification of the Aerodynamics Characteristics of an Unconventional Airfoil Using Synthetic Jet Actuators,' *AIAA Journal*, 39 (3): 361-370, 2001.

[8]Hassan, A., 'Applications of Zero-Net-Mass Jets for Enhanced Rotorcraft Aerodynamic Performance,' *Journal of Aircraft*, **38**(3): 478-485, 2001.

[9]Carter, J. E., and Soria, J., 'The Evolution of round Zero-Net-Mass-Flux Jets,' *Journal of Fluid Mechanics*, **472**: 167-200, 2002.

[10]Amitay, M., Pitt, D., Glezer, A., 'Separation Control in Duct Flows,' *Journal of Aircraft*, **39**(4): 616-620, 2002.

[11]Smith, D. R., 'The Interaction of a Synthetic Jet with a Cross-flow Boundary Layer,' *AIAA Journal*, **40**(11): 2277-2288, 2002.

[12]Amitay, M., and Glezer, A., 'Controlled Transients of Flow Reattachment over Stalled Airfoils,' *International Journal of Heat and Fluid Flow*, **23**: 690-699, 2002.

[13]Fung, P. H., and Amitay, M., 'Control of a Miniducted-Fan Unmanned Aerial Vehicle Using Active Flow Control,' *Journal of Aircraft,* **39**(4): 561-571, 2002.

[14]Bridges, A. B. and Smith, D. R., 'Influence of Orifice Orientation on a Synthetic Jet Boundary Layer Interaction,' *AIAA Journal,* **41**(12): 2394-2402, 2003.

[15]Smith, B. L., and Swift, G. W., 'A Comparison Between Synthetic Jets and Continuous Jets,' *Experiments in Fluids*, **34**: 467, 2003.

[16]Gordon, M., and Soria, J., 'PIV Measurements of a Zero-Net-Mass-Flux Jet in Cross Flow,' *Experiments in Fluids*, 33: 863-872, 2002.

[17]Schaeffler, N. W., 'The Interaction of a Synthetic Jet and a Turbulent Boundary Layer,' AIAA Paper 2003-643, 41st Aerospace Sciences Meeting and Exhibit, Reno, NV, 6-9 January, 2003.

[18]Milanovic, I. M., and Zaman, K.B.M.Q., 'Synthetic Jets in Cross-Flow,' accepted for publication in *AIAA Journal*

[19]Gordon, M., Cater, J. E., and Soria, J., 'Investigation of the Mean Passive Scalar Field in Zero-Net-Mass-Flux Jets in Cross-Flow Using Planar-Laser-Induced Fluorescence,' *Physics of Fluids*, **16**(3): 794-808, 2004.

[20]Rumsey, C., Langley Research Center Workshop 'CFD Validation of Synthetic Jets and Turbulent Separation Control,' URL: http://cfdval2004.larc.nasa.gov/ [cited 22 October 2003].

[21]Schaeffler, N., "The Isolated Synthetic Jet in Cross-flow: A Benchmark for Flow Control Simulation," AIAA Paper 04-2219, 2nd AIAA Flow Control Conference, Portland, OR, June 28, 2004.

[22]Rumsey, C., Gatski, T., and Sellers, W., 'Summary of the 2004 CFD Validation Workshop on Synthetic Jets and Turbulent Separation Control,' AIAA Paper 04-2217, AIAA Flow Control Conference, Portland, OR, June 28, 2004.

[23]Rumsey, C.L., Schaeffler, N.W., Milanovic, I. M., and Zaman, K.B.M.Q., 'Time-Accurate Computations of Isolated Circular Synthetic Jets in Cross-Flow,' submitted for presentation at the AIAA 35th Fluid Dynamics Conference, Toronto, June 6-9, 2005.

[24]Milanovic, I. M., and Zaman, K. B. M. Q., 'Fluid Dynamics of Highly Pitched and Yawed Jets in Cross-Flow,' *AIAA Journal*, **42**(5), 2004.

[25]Krist, S. L., Biedron, R. T., and Rumsey, C. L., 'CFL3D User's Manual (Version 5.0),' NASA TM-1998-208444, June 1998.

[26]Weiss, J. M. and Smith, W. A., 'Preconditioning Applied to Variable and Constant Density Flows,' *AIAA Journal*, **33**(11): 2050-2057, 1995.

[27]Roe, P. L., 'Approximate Riemann Solvers, Parameter Vectors, and Difference Schemes,' *Journal of Computational Physics*, **43**: 357-372, 1981.

[28]Spalart, P. R., and Allmaras, S. R., 'A One-Equation Turbulence Model for Aerodynamic Flows,' *La Recherche Aerospatiale*, **(1)**: 5-21, 1994.

[29]Rumsey, C. L., 'Computation of a Synthetic Jet in a Turbulent Cross-Flow Boundary Layer,' NASA/TM-2004-213273, October 2004.
[30]Milanovic, I. M., and Zaman, K. B. Q. Z, 'An Experimental Study of Synthetic Jets from Rectangular Orifices,' HT-FED2004-56825, ASME Heat Transfer/Fluids Engineering Summer Conference, Charlotte, NC, July 11-15, 2004.